

## Orbital contribution to the regulation of the spin-valley coupling in antiferromagnetic monolayer MnPTE<sub>3</sub>

Wenzhe Zhou <sup>1</sup>, Guibo Zheng,<sup>1</sup> Aolin Li,<sup>2</sup> Dehe Zhang,<sup>1</sup> and Fangping Ouyang <sup>1,2,3,\*</sup>

<sup>1</sup>*School of Physics and Electronics, Hunan Key Laboratory for Super-Microstructure and Ultrafast Process, and Hunan Key Laboratory of Nanophotonics and Devices, Central South University, Changsha 410083, People's Republic of China*

<sup>2</sup>*School of Physics and Technology, State Key Laboratory of Chemistry and Utilization of Carbon Based Energy Resources, Xinjiang University, Urumqi 830046, People's Republic of China*

<sup>3</sup>*State Key Laboratory of Powder Metallurgy, and Powder Metallurgy Research Institute, Central South University, Changsha 410083, People's Republic of China*



(Received 18 November 2022; revised 9 January 2023; accepted 12 January 2023; published 23 January 2023)

In addition to the ferromagnetic materials with inversion symmetry breaking, the symmetric antiferromagnetic materials also exhibit intrinsic valley splitting due to the spin-valley coupling. Using first-principles calculations, we investigated the manipulation of valley splitting of antiferromagnetic monolayer MnPTE<sub>3</sub> via biaxial strain. It is shown that two MnPTE<sub>3</sub> monolayers with different structures are both stable antiferromagnetic semiconductors, and exhibit valley splitting between  $K$  and  $K'$ . The spin-valley coupling strength can be greatly tuned by in-plane strain, which is due to the changes of orbital composition of electronic state and the different contribution of two sublattice atoms. The proportions of  $d$  orbitals of Mn atoms determine the orbital angular momentum of the electronic state, and the different contribution of different sublattices results in the change of Berry curvature at  $K$  and  $K'$  points. The combination of two factors leads to the same changes of valley splitting and the proportion of the  $d_{xz}$ ,  $d_{yz}$  orbitals. These results of are some significance for the design of materials with greater valley splitting and the understanding of its mechanism.

DOI: [10.1103/PhysRevB.107.035139](https://doi.org/10.1103/PhysRevB.107.035139)

### I. INTRODUCTION

As a degree of freedom that can be manipulated, valley has recently received extensive attention, largely due to the discovery and successful preparation of rich two-dimensional materials [1]. Using valley to realize information generation, processing, and storage has become a new research direction of electronics, as valleytronics. Compared with traditional electronic devices, valleytronic devices have the advantages of low power consumption and high speed [2].

Transition-metal dichalcogenides are typical valleytronic materials. The symmetry breaking of spatial inversion of transition-metal dichalcogenides leads to the nonequivalent valleys of  $K$  and  $K'$  points in the reciprocal space [3]. They exhibit opposite Berry curvature and selective absorption of chiral light. With spin-orbit coupling, the Berry curvature is equivalent to a magnetic field of the reciprocal space, and the valleys of  $K$  and  $K'$  points produce opposite spin splitting, which is characterized by spin-valley locking. The nonequivalent valleys exist generally in some systems with broken symmetry [4]. However, for molybdenum- or tungsten-based chalcogenide compounds such as intrinsic monolayer MoS<sub>2</sub> and WTe<sub>2</sub>, spin-polarized valleys are degenerate, due to time-inversion symmetry. In order to promote the wide application of valleytronic devices, valley splitting or unbalanced valley carriers are needed. Many methods have been applied, such

as external magnetic field [5,6], proximity effect [7–9], light excitation [10,11], etc. On the other hand, searching for two-dimensional materials with intrinsic large valley splitting is also the top priority in the development of valleytronics and the application of valleytronic devices.

The first solution that comes to mind is the materials with broken time-reversal symmetry. The researchers discovered the existence of intrinsic valley splitting in ferromagnetic materials with broken spatial inversion symmetry, known as ferrovalley materials. A variety of two-dimensional ferrovalley materials have been predicted, including VSe<sub>2</sub> [12], LaH<sub>2</sub> [13], GdX<sub>2</sub> ( $X = \text{F, Cl, Br}$ ) [14], RuCl<sub>2</sub> [15], Cr<sub>2</sub>COF [16], VSi<sub>2</sub>P<sub>4</sub> [17,18], GdI<sub>2</sub> [19], etc. It has also been studied to increase the ferrovalley splitting by other means, such as external electric field [20], strain [21], and spin orientation [22]. On the one hand, the valley splitting is determined by the atomic orbital composition of the valley state, which affects the orbital angular momentum. On the other hand, external conditions regulate valley splitting by changing Berry curvature.

Feng *et al.* found the intrinsic valley splitting in the antiferromagnetic material MnPSe<sub>3</sub> [23]. Although the monolayer MnPSe<sub>3</sub> has central inversion symmetry, its Hamiltonian will remain unchanged only when time inversion and spatial inversion are performed simultaneously, showing spin-valley coupling. However, only a few of the intrinsic valley splittings in antiferromagnetic materials were studied subsequently [24], and more work has been performed to destroy the spin degeneracy of valley in antiferromagnet through

\*ouyangfp06@tsinghua.org.cn

heterostructure stacking [25–28]. Previous studies have shown that  $d_{xz}$  and  $d_{yz}$  orbitals play the dominant role to the strength of spin-orbit coupling [29], but the physics in the regulation of antiferromagnetic intrinsic spin-valley coupling is still unclear.

Here, we consider two crystal structures of monolayer MnPTE<sub>3</sub> to study the mechanism of valley splitting, in which the crystalline field will lead to different orbital splitting. Based on first-principle studies, the structural stability and electronic structures of MnPTE<sub>3</sub> monolayers are analyzed. The electronic states of the top valence band (TVB) and bottom conduction band (BCB) are mainly composed of the  $d_{x^2-y^2}$ ,  $d_{xy}$ , and  $d_{xz}$ ,  $d_{yz}$  orbitals of Mn atoms and the  $p_x$ ,  $p_y$  orbitals of Te atoms. Biaxial strain can effectively change the interaction between  $p$  and  $d$  orbitals, thus regulating the contribution of  $d$  orbitals. The energy valley splitting is mainly determined by the ratio of  $d_{xz}$ ,  $d_{yz}$  orbitals, which have the same variation law with strain. Due to the larger spin-orbit coupling of Mn atom, by analyzing the effective Hamiltonian, we deduced the relationship between the valley splitting and the proportion of the  $d_{x^2-y^2}$ ,  $d_{xy}$ , and  $d_{xz}$ ,  $d_{yz}$  orbitals, respectively, which is consistent with the results of the first-principle calculations.

## II. COMPUTATIONAL DETAILS

The calculations of electronic structures in this work are performed through the Vienna *ab initio* Simulation Package (VASP), which is based on density-functional theory (DFT) [30], and is convenient for studying the electronic properties of various materials. The projector augmented-wave scheme is used and the energy cutoff of the plane-wave basis is set to be 600 eV [31]. The exchange-correlation effect is treated by the generalized gradient approximation of Perdew-Burke-Ernzerhof functional [32]. The structural optimization is stopped after the force on each atom is less than 0.001 eV/Å, and the energy criterion of electronic self-consistent iteration is  $10^{-6}$  eV. The  $\Gamma$ -centered  $k$ -point grid of  $11 \times 11 \times 1$  is adopted. A vacuum region of 25 Å is applied along the  $z$  direction, which is enough for ignoring the interaction between repeated slabs. The on-site Coulomb interaction for the  $d$  orbital of Mn atom is added with the parameter  $U = 4$  eV [33]. The phonon spectrum is calculated using the density functional perturbation theory (DFPT) method combined with the PHONOPY tools [34]. A  $3 \times 3 \times 1$  superlattice is used to calculate the dynamical matrix. The calculation of Berry curvature in reciprocal space is carried out as implemented in the WANNI90 package [35].

## III. RESULTS AND DISCUSSION

In monolayer MnPTE<sub>3</sub>, there are six Te atoms nearest to each Mn atom. In past studies, the coordination environment was octahedral, which is similar to the 1T phase of transition-metal dichalcogenides. Here, we constructed another structure of monolayer MnPTE<sub>3</sub>, in which the coordination environment is triangular prism. The two structures of monolayer MnPTE<sub>3</sub> are shown in Fig. 1, which are, respectively, labeled as  $T$ -MnPTE<sub>3</sub> and  $H$ -MnPTE<sub>3</sub>. Monolayer  $T$ -MnPTE<sub>3</sub> is center-inversion symmetric with the point group of  $D_{3d}$ , and  $H$ -MnPTE<sub>3</sub> is mirror symmetric about the plane of Mn

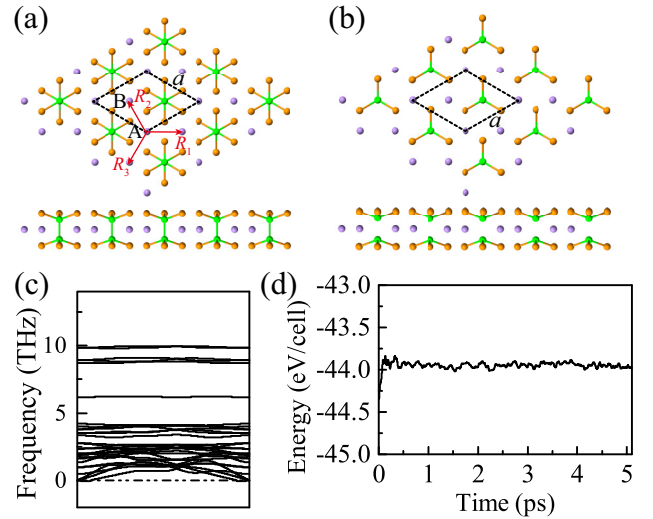


FIG. 1. (a), (b) Top and side views of monolayer MnPTE<sub>3</sub> with octahedral structure ( $T$ -MnPTE<sub>3</sub>) and trigonal prismatic structure ( $H$ -MnPTE<sub>3</sub>). (c) Phonon spectrum of monolayer  $H$ -MnPTE<sub>3</sub>. (d) Variation of energy per unit cell of monolayer  $H$ -MnPTE<sub>3</sub> with time during *ab initio* molecular simulation at room temperature.

atoms with the point group of  $D_{3h}$ . The lattice constants, bond lengths, and ground-state energies of monolayer MnPTE<sub>3</sub> are listed in Table I. The lattice constant of  $H$ -MnPTE<sub>3</sub> is smaller than that of  $T$ -MnPTE<sub>3</sub>, but the bond length between Mn and Te is longer. As expected, the ground states of monolayer  $T$ -MnPTE<sub>3</sub> and  $H$ -MnPTE<sub>3</sub> are both antiferromagnetic.

The dynamic and thermodynamic stability are verified for  $H$ -MnPTE<sub>3</sub>. The phonon spectrum and result of molecular dynamics are shown in Fig. 1. There is no imaginary frequency and the average energy per atom varies in the range of  $2/3k_B T$ , indicating that monolayer  $H$ -MnPTE<sub>3</sub> can exist stably, although its ground-state energy is higher than that of  $T$ -MnPTE<sub>3</sub>.

The electronic structures of  $T$ -MnPTE<sub>3</sub> and  $H$ -MnPTE<sub>3</sub> monolayers are studied. As shown in Fig. 2, both  $T$ -MnPTE<sub>3</sub> and  $H$ -MnPTE<sub>3</sub> are antiferromagnetic semiconductors. Without spin-orbit coupling, the band gap of monolayer  $T$ -MnPTE<sub>3</sub> is direct with the valence-band maximum and the conduction-band minimum at  $K$  and  $K'$  points. After considering spin-orbit coupling, the states of  $K$  and  $K'$  points are not energy degenerate but the spin is still degenerate. The states near Fermi level are hybridized by the  $d$  orbitals of Mn atoms and the  $p$  orbitals of Te atoms. The  $p_x$  and  $p_y$  orbitals of Te atoms contribute to both the top valence band and the bottom conduction band. The TVB is mainly composed of  $d_{xz}$  and  $d_{yz}$  orbitals, but the BCB is contributed by  $d_{x^2-y^2}$  and  $d_{xy}$  orbitals. For  $T$ -MnPTE<sub>3</sub>, there is more hybridization between  $d$  orbitals, while the  $d_{x^2-y^2}$ ,  $d_{xy}$  and  $d_{xz}$ ,  $d_{yz}$  orbitals in  $H$ -MnPTE<sub>3</sub> are separated. The reason may be that the longer bond length in  $H$ -MnPTE<sub>3</sub> leads to the weaker interaction between  $d$  orbitals and  $p$  orbitals, since there is no direct interaction between the  $d_{x^2-y^2}$ ,  $d_{xy}$  and  $d_{xz}$ ,  $d_{yz}$  orbitals.

The valley splitting in antiferromagnet is caused by spin-valley coupling. The system is symmetric only under the operation of simultaneous time reversal and spatial inversion.

TABLE I. In-plane lattice parameters ( $a$ ), bond lengths, and ground-state energies ( $E_0$ ) of monolayer MnPTE<sub>3</sub>.

	$a$ (Å)	$l_{\text{Mn-Te}}$ (Å)	$l_{\text{P-Te}}$ (Å)	$l_{\text{P-P}}$ (Å)	$E_0$ (eV)	
					FM	AFM
$T$ -MnPTE <sub>3</sub>	6.986	2.96	2.47	2.27	-45.693	-45.728
$H$ -MnPTE <sub>3</sub>	6.847	2.99	2.47	2.42	-44.986	-45.033

For spin up, it corresponds to one magnetic atomic sublattice and lacks spatial inversion symmetry, so the states at  $K$  and  $K'$  have opposite orbital magnetic moments and Berry curvature. As for spin down, it is occupied by another sublattice and its Berry curvature is opposite to the spin-up state. The calculated Berry curvatures in reciprocal space are in good agreement with the conclusion of symmetry analysis, as shown in Fig. 3. For monolayer  $T$ -MnPTE<sub>3</sub>, the Berry curvature for the spin-up states at the top valence band is negative near  $K$  point and positive near  $K'$  point, leading to the valley Hall effect of spin up. The opposite occurs for the Berry curvature of the spin-down states, which will give rise to the valley Hall effect with an inverted sign. The Berry curvatures for the bottom conduction band and the top valence band at the same spin and  $K$  point have the same sign. A similar situation occurs for the TVB of monolayer  $H$ -MnPTE<sub>3</sub>, but the Berry curvature for the BCB has the opposite sign with that for the TVB. The Berry curvature is equivalent to the magnetic field of the inverted space. Therefore, the energy levels of spin-up and spin-down states at the bottom conduction band of  $K$  point move upward under the opposite equivalent magnetic field, and the energy levels at  $K'$  point move downward. Finally, spin-degenerate valley splitting occurs in the antiferromagnetic material with

spatial inversion symmetry. The valley Hall effect and the spin Hall effect in monolayer MnPTE<sub>3</sub> are coupled, and the valley Hall effect caused by Berry curvature is usually accompanied by the orbital Hall effect, which is worth studying.

The spin-orbit coupling strength of the electronic state depends largely on the composition of  $d$  orbitals. For MnPTE<sub>3</sub> monolayers, the compositions of  $d_{x^2-y^2}$ ,  $d_{xy}$  and  $d_{xz}$ ,  $d_{yz}$  orbitals are determined by their interactions with the  $p$  orbitals of Te atoms, which can be greatly tuned by in-plane strain. The regulations of band edge, band gap, valley splitting, and compositions of  $d$  orbitals via strain are shown in Fig. 4. The tensile strain will reduce the energy of the band edge. The deformation potential (DP) is calculated based on the first derivative of band-edge energy to strain,  $E_{\text{DP}} = \partial E_{\text{edge}} / \partial (\Delta a / a_0)$ , which is the sum of deformation potentials in  $x$  and  $y$  directions. The DPs of the bottom conduction band at  $K$  and  $K'$  points are  $-0.735$  and  $-1.503$  eV, respectively, which are smaller than those of the top valence band at  $K$  ( $-5.648$  eV) and  $K'$  points ( $-4.268$  eV). The difference of deformation potential between  $K$  and  $K'$  points reflects that different valleys will have different electron-phonon interactions. The compression strain will reduce the energy gap at  $K$  and  $K'$  points, because the conduction band is composed of

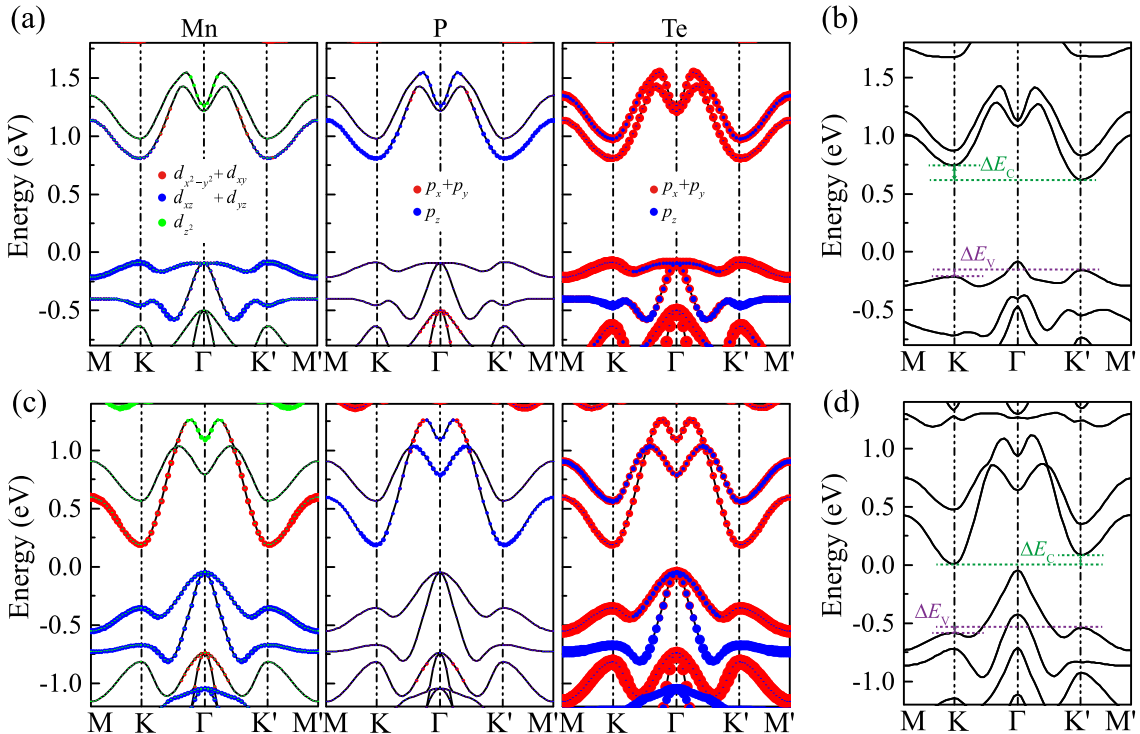


FIG. 2. Band structures of monolayer  $T$ -MnPTE<sub>3</sub> without (a) and with (b) spin-orbit coupling. Band structures of monolayer  $H$ -MnPTE<sub>3</sub> without (c) and with (d) spin-orbit coupling.

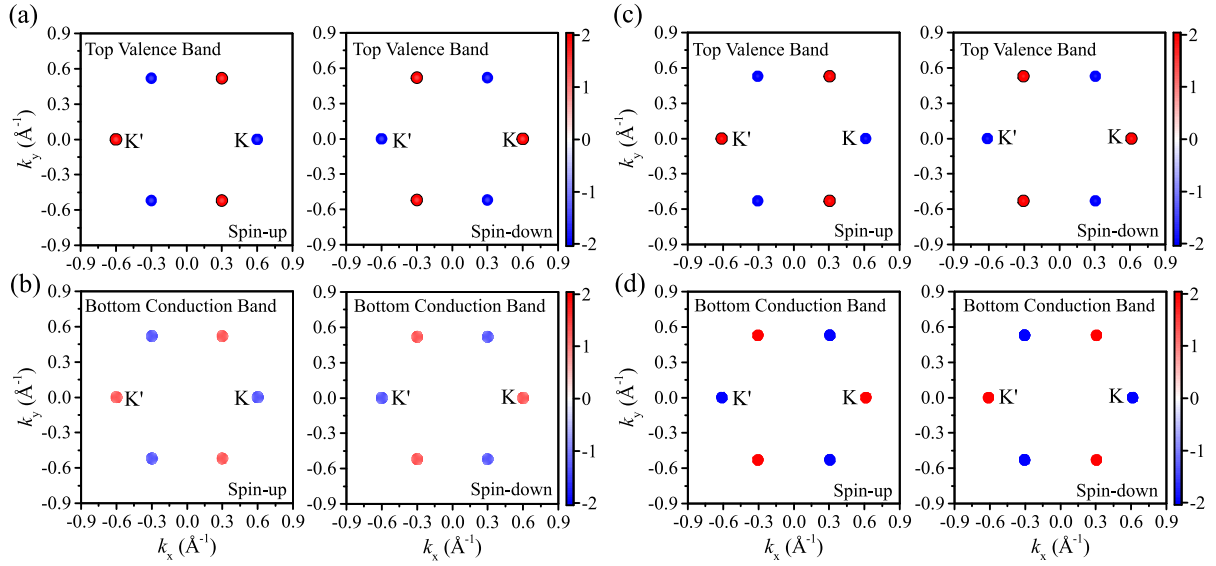


FIG. 3. Spin-dependent Berry curvatures near  $K$  and  $K'$  points of the top valence band and the bottom conduction band of monolayer  $T\text{-MnPTE}_3$  (a), (b) and  $H\text{-MnPTE}_3$  (c), (d).

more  $d_{x^2-y^2}$ ,  $d_{xy}$  orbitals and the energy of its bonding state decreases under the stronger in-plane interaction.

For monolayer  $H\text{-MnPTE}_3$ , the valley splittings of both the conduction band and the valence band will increase under the compression strain. However, for monolayer  $T\text{-MnPTE}_3$ , the valley splitting of the TVB will also decrease with the increase of the lattice, but the splitting of the BCB will first increase and then decrease. From Figs. 4(c) and 4(d), it is found that the regulation of valley splitting comes from the changes of the compositions of  $d$  orbitals, and the change of valley splitting is the same as that of  $d_{xz}$  and  $d_{yz}$  orbitals.

From the perspective of orbital angular momentum, the valley splitting is indeed proportional to the compositions of  $d_{x^2-y^2}$ ,  $d_{xy}$ , and  $d_{xz}$ ,  $d_{yz}$  orbitals, respectively. However, the  $z$ -direction orbital angular momentum of the  $d_{\pm 1}$  orbital composed of  $d_{xz}$  and  $d_{yz}$  orbitals is half of the  $z$ -direction orbital angular momentum of the  $d_{\pm 2}$  orbital composed of  $d_{x^2-y^2}$  and  $d_{xy}$  orbitals. The contribution of  $d_{x^2-y^2}$  and  $d_{xy}$  orbitals to the valley splitting with out-of-plane spin polarization should be greater than that of  $d_{xz}$  and  $d_{yz}$  orbitals. Therefore, there are other factors that will affect the valley splitting.

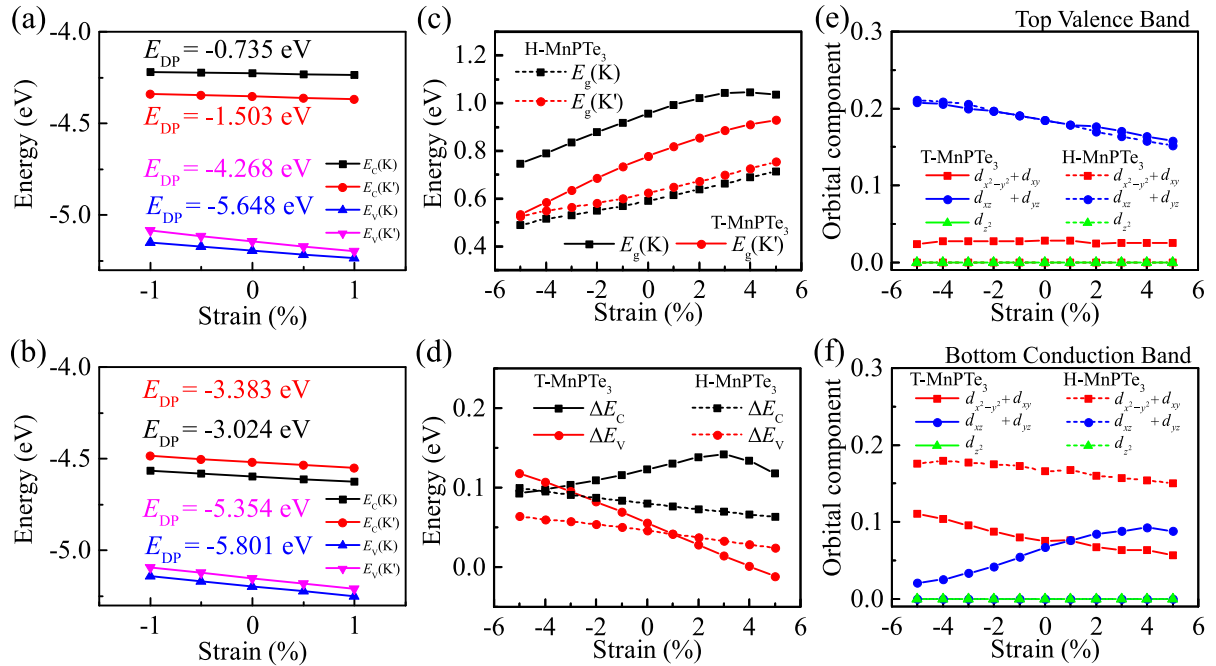


FIG. 4. Effect of strain on the band edge for extracting the deformation potentials ( $E_{DP}$ ) of monolayer  $T\text{-MnPTE}_3$  (a) and  $H\text{-MnPTE}_3$  (b). (c) Strain-regulated band gaps at  $K$  and  $K'$  points. (d) Tuning the valley splittings of top valence band and bottom conduction band via in-plane biaxial strain. Changes of  $d$ -orbital compositions at  $K$  point of the TVB (e) BCB (f) of monolayer  $\text{MnPTE}_3$  as functions of the biaxial strain. Solid line and dotted line represent  $T\text{-MnPTE}_3$  and  $H\text{-MnPTE}_3$ , respectively.

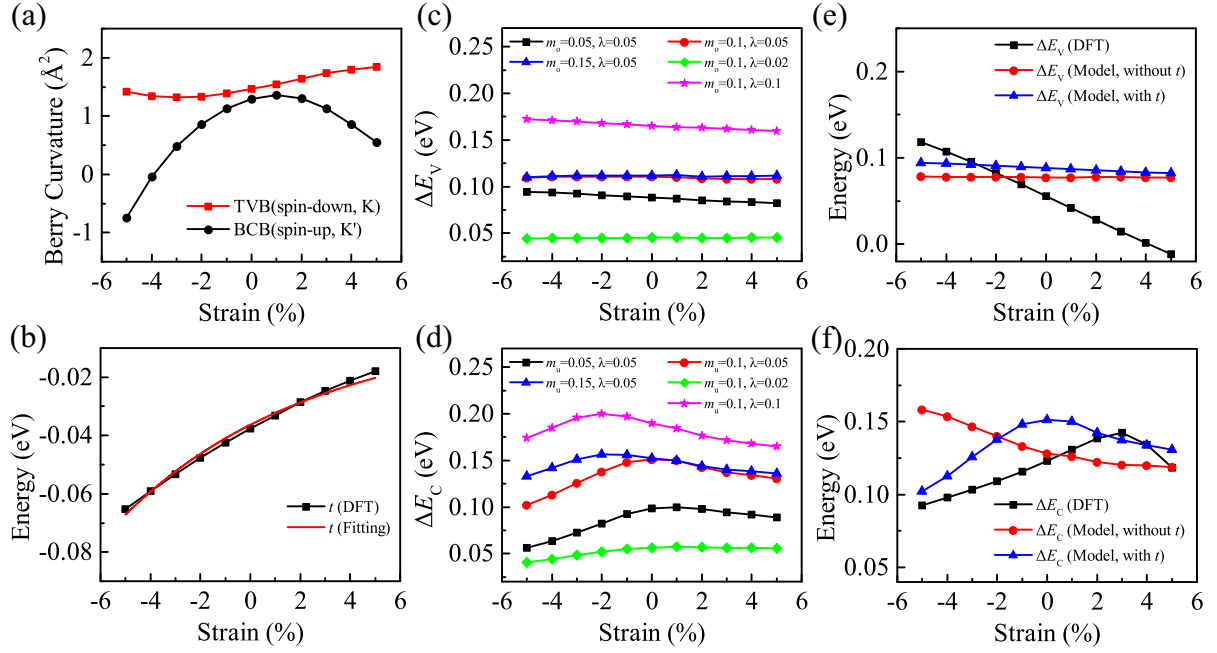


FIG. 5. (a) Strain-regulated Berry curvature at  $K$  or  $K'$  point of the top valence band and bottom conduction band. (b) Change of hopping parameter  $t$  as a function of the in-plane biaxial strain. Valley splitting at the TVB (c) and the BCB (d) with different spin-splitting energy and spin-orbit coupling strength. Comparisons between the valley splitting at the TVB (e) and the BCB (f) obtained from the effective Hamiltonian model with or without  $t$  and the first-principle calculation, when the parameters are  $m_o = 0.05$  eV,  $m_u = 0.1$  eV, and  $\lambda = 0.05$  eV.

In order to illustrate the effect of another factor on valley splitting, an effective Hamiltonian model is built. The basis set is selected to be

$$\begin{aligned}
 |u\rangle^{(A)} &= u_1|d_{\tau_1}\rangle^{(A)} + u_2|d_{\tau_2}\rangle^{(A)} \\
 |o\rangle^{(A)} &= o_1|d_{-\tau_1}\rangle^{(A)} + o_2|d_{-\tau_2}\rangle^{(A)} \\
 |u\rangle^{(B)} &= u_1|d_{-\tau_1}\rangle^{(B)} + u_2|d_{-\tau_2}\rangle^{(B)}, \\
 |o\rangle^{(B)} &= o_1|d_{\tau_1}\rangle^{(B)} + o_2|d_{\tau_2}\rangle^{(B)}
 \end{aligned} \quad (1)$$

where  $\tau = \pm$  is the valley index.  $|u\rangle$  and  $|o\rangle$  represent the wave functions of the unoccupied state and the occupied state, respectively, and the superscripts  $(A)$  and  $(B)$  stand for the contributions of sublattices  $A$  and  $B$ , respectively. The changed orbital compositions ( $u_1, u_2, o_1, o_2$ ) reflect the influence of the  $p$  orbital of Te atom on the  $d$  orbital of Mn atom, and they are obtained from the results of orbital compositions calculated from DFT. The Hamiltonian without spin degree of freedom can be written as

$$H_0 = \begin{bmatrix} \Delta_u & 0 & 3|u_2|^2 t & 0 \\ 0 & \Delta_o & 0 & 3|o_2|^2 t \\ 3|u_2|^2 t & 0 & \Delta_u & 0 \\ 0 & 3|o_2|^2 t & 0 & \Delta_o \end{bmatrix}, \quad (2)$$

in which

$$\Delta_u = |u_1|^2 \Delta_1 + |u_2|^2 \Delta_2, \quad \Delta_o = |o_1|^2 \Delta_1 + |o_2|^2 \Delta_2. \quad (3)$$

$\Delta_1$  and  $\Delta_2$  are the on-site energies of  $d_{xz}$ ,  $d_{yz}$  and  $d_{x^2-y^2}$ ,  $d_{xy}$  orbitals, respectively, which are expressed as

$$\begin{aligned}
 \Delta_1 &= \langle d_{\tau_1} | H | d_{\tau_1} \rangle^{(A,A)} = \langle d_{\tau_1} | H | d_{\tau_1} \rangle^{(B,B)} \\
 \Delta_2 &= \langle d_{\tau_2} | H | d_{\tau_2} \rangle^{(A,A)} = \langle d_{\tau_2} | H | d_{\tau_2} \rangle^{(B,B)}.
 \end{aligned} \quad (4)$$

The parameter  $t$  is derived from hopping energies of  $d_{x^2-y^2}$ ,  $d_{xy}$  orbitals between  $A$  and  $B$  sublattices, as follows:

$$t = \langle d_{\tau_2}(\vec{r}) | \hat{h}(\vec{r}) | d_{\tau_2}(\vec{r} - \vec{R}_1) \rangle, \quad (5)$$

which represents the different contributions of  $A$  and  $B$  sublattices to the electronic state caused by the interaction between Mn atoms. The parameter  $t$  can be extracted from the hopping integral between the fitted Wannier functions, and its change with strain is shown in Fig. 5(b). The change of hopping parameter with the strain satisfies the empirical scaling rule of the form [36]

$$t = t_0(1 + \varepsilon)^{-n}. \quad (6)$$

After fitting, the hopping parameter  $t_0 = -0.036$  eV, and the exponent  $n = 12$  for monolayer  $T$ -MnPTe<sub>3</sub>. The parameter  $t$  is a negative value, and increases with tensile strain, indicating that the interaction between  $A$  and  $B$  sublattices should be stronger when the lattice parameter is smaller.

In the two structures of monolayer MnPTe<sub>3</sub>, the coordination environment between Mn atoms is the same, so the effective Hamiltonian model is applicable to the two structures. The difference lies in the size of the orbital compositions ( $u_1, u_2, o_1, o_2$ ) and interaction between  $d$  orbitals ( $t$ ). Since the variation of valley splitting of the top valence band and bottom conduction band of monolayer  $H$ -MnPTe<sub>3</sub> with strain is the same as that of the TVB of monolayer  $T$ -MnPTe<sub>3</sub>,

we only use the effective model to discuss the regulation mechanism of valley splitting of monolayer  $T$ -MnPTe<sub>3</sub>.

Considering the on-site spin-orbit coupling and antiferromagnetic order, the Hamiltonian can be written as

$$H = H_0 \otimes \sigma_0 + \begin{bmatrix} m_u & 0 \\ 0 & m_o \end{bmatrix} \otimes s_z \otimes \sigma_z + \lambda(L_x \otimes \sigma_x + L_y \otimes \sigma_y + L_z \otimes \sigma_z), \quad (7)$$

where  $\sigma_x$ ,  $\sigma_y$ ,  $\sigma_z$ , and  $\sigma_0$  are the Pauli vectors and identity matrix for spin space.  $m_u$  and  $m_o$  are splitting energies of polarized spin at the unoccupied and occupied bands.  $\lambda$

characterizes the strength of the spin-orbit coupling. The orbital angular momenta in the bases of formula (1) can be expressed as,

$$L_x = \begin{bmatrix} 2u_1u_2 & 0 & 0 & 0 \\ 0 & 2o_1o_2 & 0 & 0 \\ 0 & 0 & 2u_1u_2 & 0 \\ 0 & 0 & 0 & 2o_1o_2 \end{bmatrix}, \quad (8)$$

$$L_y = 0,$$

and

$$L_z = \begin{bmatrix} \tau(u_1u_1 + 2u_2u_2) & 0 & 0 & 0 \\ 0 & -\tau(o_1o_1 + 2o_2o_2) & 0 & 0 \\ 0 & 0 & -\tau(u_1u_1 + 2u_2u_2) & 0 \\ 0 & 0 & 0 & \tau(o_1o_1 + 2o_2o_2) \end{bmatrix}. \quad (9)$$

Solving the eigenequation of the Hamiltonian of formula (6), we obtain the energies of the TVB and the BCB, as follows:

$$\varepsilon_{TVB} = \Delta_o + \sqrt{(m_o - \tau\lambda(|o_1|^2 + 2|o_2|^2))^2 + (3|o_2|^2t + \lambda 2o_1o_2)^2}, \quad (10)$$

and

$$\varepsilon_{BCB} = \Delta_u - \sqrt{(m_u + \tau\lambda(|u_1|^2 + 2|u_2|^2))^2 + (3|u_2|^2t + \lambda 2u_1u_2)^2}. \quad (11)$$

So, the valley splitting at the TVB and the BCB can be expressed as

$$\Delta E_V = |\sqrt{(m_o + \lambda(|o_1|^2 + 2|o_2|^2))^2 + (\lambda 2o_1o_2 + 3|o_2|^2t)^2} - \sqrt{(m_o - \lambda(|o_1|^2 + 2|o_2|^2))^2 + (\lambda 2o_1o_2 + 3|o_2|^2t)^2}|, \quad (12)$$

and

$$\Delta E_C = |\sqrt{(m_u - \lambda(|u_1|^2 + 2|u_2|^2))^2 + (3|u_2|^2t + \lambda 2u_1u_2)^2} - \sqrt{(m_u + \lambda(|u_1|^2 + 2|u_2|^2))^2 + (3|u_2|^2t + \lambda 2u_1u_2)^2}|. \quad (13)$$

Here, only different orbital contributions to the valley splitting are discussed, which are reflected by the tunable parameters of the orbital compositions ( $u_1$ ,  $u_2$ ,  $o_1$ ,  $o_2$ ) and interaction between d orbitals ( $t$ ), so the parameters  $m_o$ ,  $m_u$ , and  $\lambda$  are set to be unchanged with strain. The parameter-determined regulation laws are shown in Figs. 5(c) and 5(d). With larger spin-splitting energy  $m_o$  and  $m_u$ , the valley splitting is larger and the decrease with tensile strain is smaller. The stronger spin-orbit coupling has a similar effect, but the decrease with compression strain is larger for the bottom conduction band. Only when the parameters are appropriate, the variation law obtained by the effective model is similar to that calculated by DFT.

In order to compare with the results of DFT calculation and explain the effect of parameter  $t$  on valley splitting, we choose  $m_o = 0.05$  eV,  $m_u = 0.1$  eV, and  $\lambda = 0.05$  eV. As shown in Figs. 5(e) and 5(f), if the interaction between sublattices is not considered, the valley splitting at the bottom conduction band decreases with the tensile strain, and after considering the parameter  $t$ , the valley splitting increases first and then decreases. The parameter  $t$  will lead to different contributions

of sublattices  $A$  and  $B$  to a state, which is equivalent to affecting the different energies of a certain spin state in  $A$  and  $B$  sublattices. The asymmetry of the sublattice affects the Berry curvature of the valley, which makes the Berry curvature of the valley at the BCB first increase and then decrease. The Berry curvature at the TVB is opposite to that at the BCB, which decreases first and then increases. However, the composition of  $d_{xz}$  and  $d_{yz}$  orbitals decreases significantly, making the valley splitting at the TVB to decrease with the tensile strain. The valley splitting at the TVB described by the effective Hamiltonian model has little change, which is due to the improper parameters and their change with strain. The effect of parameter  $t$  does make the change of valley splitting closer to the result calculated by DFT.

#### IV. CONCLUSIONS

In summary, using first-principles research based on DFT, we investigated the valley splitting of antiferromagnetic monolayer MnPTe<sub>3</sub>. MnPTe<sub>3</sub> monolayers with two different structures which are both stable antiferromagnetic

semiconductors, and exhibit valley splitting energy of  $45.8 \sim 123$  meV between  $K$  and  $K'$ . Only the valley splitting at the BCB of monolayer  $T$ -MnPTe<sub>3</sub> increases first and then decreases with the tensile strain. The regulation of valley splitting can be understood through the changes of orbital composition of electronic state and the contribution of two sublattice atoms. The proportions of  $d$  orbitals of Mn atoms determine the orbital angular momentum of the electronic state, and its change comes from the interaction between the  $d$  orbitals of Mn atoms and in-plane  $p$  orbitals of Te atoms. The interaction between  $d$  orbitals of two Mn atomic sublattices dominates the potential difference of spin up or spin down at different sublattices, resulting in the change of Berry curvature at  $K$  and  $K'$  points. The combination of two factors leads

to the same changes of valley splitting and the proportion of the  $d_{xz}$  and  $d_{yz}$  orbitals.

### ACKNOWLEDGMENTS

This work is financially supported by the National Natural Science Foundation of China (Grants No. 52073308, No. 12104514, and No. 12164046), the Central South University Research Fund for Sheng-hua scholars (Grant No. 502033019), and China Postdoctoral Science Foundation (Grant No. 2022TQ0379). This work was carried out in part using computing resources at the High Performance Computing Center of Central South University.

- 
- [1] J. R. Schaibley, H. Yu, G. Clark, P. Rivera, J. S. Ross, K. L. Seyler, W. Yao, and X. Xu, Valleytronics in 2D materials, *Nat. Rev. Mater.* **1**, 16055 (2016).
- [2] S. A. Vitale, D. Nezich, J. O. Varghese, P. Kim, N. Gedik, P. Jarillo-Herrero, D. Xiao, and M. Rothschild, Valleytronics, opportunities, challenges, and paths forward, *Small* **14**, 1801483 (2018).
- [3] C. Jiang, F. Liu, J. Cuadra, Z. Huang, K. Li, A. Rasmita, A. Srivastava, Z. Liu, and W.-B. Gao, Zeeman splitting via spin-valley-layer coupling in bilayer MoTe<sub>2</sub>, *Nat. Commun.* **8**, 802 (2017).
- [4] W. Zhou, L. Wu, A. Li, B. Zhang, and F. Ouyang, Structural symmetry, spin-orbit coupling, and valley-related properties of monolayer WSi<sub>2</sub>N<sub>4</sub> family, *J. Phys. Chem. Lett.* **12**, 11622 (2021).
- [5] X. X. Zhang, Y. Lai, E. Dohner, S. Moon, T. Taniguchi, K. Watanabe, D. Smirnov, and T. F. Heinz, Zeeman-Induced Valley-Sensitive Photocurrent in Monolayer MoS<sub>2</sub>, *Phys. Rev. Lett.* **122**, 127401 (2019).
- [6] D. MacNeill, C. Heikes, K. F. Mak, Z. Anderson, A. Kormányos, V. Zólyomi, J. Park, and D. C. Ralph, Breaking of Valley Degeneracy by Magnetic Field in Monolayer MoSe<sub>2</sub>, *Phys. Rev. Lett.* **114**, 037401 (2015).
- [7] L. Xu, M. Yang, L. Shen, J. Zhou, T. Zhu, and Y. P. Feng, Large valley splitting in monolayer WS<sub>2</sub> by proximity coupling to an insulating antiferromagnetic substrate, *Phys. Rev. B* **97**, 041405 (2018).
- [8] C. Zhao, T. Norden, P. Zhang, P. Zhao, Y. Cheng, F. Sun, J. P. Parry, P. Taheri, J. Wang, Y. Yang, T. Scrace, K. Kang, S. Yang, G. Miao, R. Sabirianov, G. Kioseoglou, W. Huang, A. Petrou, and H. Zeng, Enhanced valley splitting in monolayer WSe<sub>2</sub> due to magnetic exchange field, *Nat. Nanotechnol.* **12**, 757 (2017).
- [9] W. Zhou, Z. Yang, A. Li, M. Long, and F. Ouyang, Spin and valley splittings in Janus monolayer WSSe on a MnO(111) surface: Large effective Zeeman field and opening of a helical gap, *Phys. Rev. B* **101**, 045113 (2020).
- [10] T. Cao, G. Wang, W. Han, H. Ye, C. Zhu, J. Shi, Q. Niu, P. Tan, E. Wang, B. Liu, and J. Feng, Valley-selective circular dichroism of monolayer molybdenum disulphide, *Nat. Commun.* **3**, 887 (2012).
- [11] L. Xie and X. Cui, Manipulating spin-polarized photocurrents in 2D transition metal dichalcogenides, *Proc. Natl. Acad. Sci. USA* **113**, 3746 (2016).
- [12] W. Y. Tong, S. J. Gong, X. Wan, and C. G. Duan, Concepts of ferrovalley material and anomalous valley Hall effect, *Nat. Commun.* **7**, 13612 (2016).
- [13] Y. Shi, N. Jia, J. Cai, Z. Lyu, and Z. Liu, 2D electrene LaH<sub>2</sub> monolayer: An ideal ferrovalley direct semiconductor with room-temperature ferromagnetic stability, *J. Phys.: Condens. Matter* **34**, 475303 (2022).
- [14] K. Sheng, H. K. Yuan, and Z. Y. Wang, Monolayer gadolinium halides, GdX<sub>2</sub> (X = F, Cl, Br): Intrinsic ferrovalley materials with spontaneous spin and valley polarizations, *Phys. Chem. Chem. Phys.* **24**, 3865 (2022).
- [15] K. Sheng, B. Zhang, H. K. Yuan, and Z. Y. Wang, Strain-engineered topological phase transitions in ferrovalley 2H-RuCl<sub>2</sub> monolayer, *Phys. Rev. B* **105**, 195312 (2022).
- [16] S. Li, J. He, L. Grajciar, and P. Nachtigall, Intrinsic valley polarization in 2D magnetic MXenes: Surface engineering induced spin-valley coupling, *J. Mater. Chem. C* **9**, 11132 (2021).
- [17] S. D. Guo, X. S. Guo, G. Wang, K. Cheng, and Y. S. Ang, Electric-field induced magnetic-anisotropy transformation to achieve spontaneous valley polarization, *J. Mater. Chem. C* **10**, 16363 (2022).
- [18] X. Feng, X. Xu, Z. He, R. Peng, Y. Dai, B. Huang, and Y. Ma, Valley-related multiple Hall effect in monolayer VSi<sub>2</sub>P<sub>4</sub>, *Phys. Rev. B* **104**, 075421 (2021).
- [19] H. X. Cheng, J. Zhou, W. Ji, Y. N. Zhang, and Y. P. Feng, Two-dimensional intrinsic ferrovalley GdI<sub>2</sub> with large valley polarization, *Phys. Rev. B* **103**, 125121 (2021).
- [20] D. Zhang, A. Li, X. Chen, W. Zhou, and F. Ouyang, Tuning valley splitting and magnetic anisotropy of multiferroic CuMP<sub>2</sub>X<sub>6</sub> (M = Cr, V; X = S, Se) monolayer, *Phys. Rev. B* **105**, 085408 (2022).
- [21] S. D. Guo, J. X. Zhu, W. Q. Mu, and B. G. Liu, Possible way to achieve anomalous valley Hall effect by piezoelectric effect in a GdCl<sub>2</sub> monolayer, *Phys. Rev. B* **104**, 224428 (2021).
- [22] R. Peng, Y. Ma, X. Xu, Z. He, B. Huang, and Y. Dai, Intrinsic anomalous valley Hall effect in single-layer Nb<sub>3</sub>I<sub>8</sub>, *Phys. Rev. B* **102**, 035412 (2020).

- [23] X. Li, T. Cao, Q. Niu, J. Shi, and J. Feng, Coupling the valley degree of freedom to antiferromagnetic order, *Proc. Natl. Acad. Sci. USA* **110**, 3738 (2013).
- [24] X. Xu, Z. He, Y. Dai, B. Huang, and Y. Ma, Single-valley state in a two-dimensional antiferromagnetic lattice, *Phys. Rev. B* **104**, 205430 (2021).
- [25] W. Du, R. Peng, Z. He, Y. Dai, B. Huang, and Y. Ma, Anomalous valley Hall effect in antiferromagnetic monolayers, *npj 2D Mater. Appl.* **6**, 11 (2022).
- [26] B. J. Wang, Y. Y. Sun, J. Chen, W. Ju, Y. P. An, and S. J. Gong, Valley splitting in the antiferromagnetic heterostructure MnPSe<sub>3</sub>/WSe<sub>2</sub>, *J. Mater. Chem. C* **9**, 3562 (2021).
- [27] H. Hu, W. Y. Tong, Y. H. Shen, and C. G. Duan, Electrical control of the valley degree of freedom in 2D ferroelectric/antiferromagnetic heterostructures, *J. Mater. Chem. C* **8**, 8098 (2020).
- [28] Q. Pei and W. Mi, Electrical Control of Magnetic Behavior and Valley Polarization of Monolayer Antiferromagnetic MnPSe<sub>3</sub> on an Insulating Ferroelectric Substrate from First Principles, *Phys. Rev. Appl.* **11**, 014011 (2019).
- [29] W. Zhou, J. Chen, B. Zhang, H. Duan, and F. Ouyang, Manipulation of the Rashba spin-orbit coupling of a distorted 1T-phase Janus WSSe monolayer: Dominant role of charge transfer and orbital components, *Phys. Rev. B* **103**, 195114 (2021).
- [30] G. Kresse and J. Furthmüller, Efficient iterative schemes for ab initio total-energy calculations using a plane-wave basis set, *Phys. Rev. B* **54**, 11169 (1996).
- [31] P. E. Blöchl, Projector augmented-wave method, *Phys. Rev. B* **50**, 17953 (1994).
- [32] J. P. Perdew, K. Burke, and M. Ernzerhof, Generalized Gradient Approximation Made Simple, *Phys. Rev. Lett.* **77**, 3865 (1996).
- [33] B. L. Chittari, Y. Park, D. Lee, M. Han, A. H. MacDonald, E. Hwang, and J. Jung, Electronic and magnetic properties of single-layer MPX<sub>3</sub> metal phosphorous trichalcogenides, *Phys. Rev. B* **94**, 184428 (2016).
- [34] A. Togo and I. Tanaka, First principles phonon calculations in materials science, *Scr. Mater.* **108**, 1 (2015).
- [35] A. A. Mostofi, J. R. Yates, Y. S. Lee, I. Souza, D. Vanderbilt, and N. Marzari, WANNIER90: A tool for obtaining maximally-localised Wannier functions, *Comput. Phys. Commun.* **178**, 685 (2008).
- [36] J. Arriaga, M. C. Muñoz, V. R. Velasco, and F. Garcia-Moliner, Electronic structure of strained GaAs/GaP (001) superlattices, *Phys. Rev. B* **43**, 9626 (1991).